JOURNAL OF AIRCRAFT
Vol. 34, No. 1, January–February 1997

Finite Difference Maxwell Solver to Study Geometric Shape Effects on Radar Signature

Hoang Vinh*
High Technology Corporation, Hampton, Virginia 23666
and
C. P. van Dam† and H. A. Dwyer†
University of California, Davis, Davis, California 95616-5294

The development and application of a finite difference time-domain solver for Maxwell's equations are presented. The work described here is the result of a research effort aimed at developing an accurate and efficient numerical method capable of simulating electromagnetic scattering from three-dimensional arbitrarily shaped objects to predict their radar cross sections (RCS). The finite difference formulation is presented and the accuracy of the Maxwell solver is demonstrated for several test cases. The capability of the Maxwell solver as a design and analysis tool is illustrated through a parametric study that examines the effects of systematic changes in the shape of aircraft wings on their RCS. The results indicate that for head-on radar illumination, a significant reduction in the RCS of a wing can be achieved by sweeping its leading edge and varying its spanwise thickness.

Nomenclature

c	=	wave speed, $1/\sqrt{\mu\varepsilon}$
$\boldsymbol{E}$	=	electric-field intensity vector in time domain
$\tilde{\boldsymbol{E}}$	=	electric-field intensity vector in frequency domain
E_0	=	incident wave amplitude
$\boldsymbol{H}$	=	magnetic-field intensity vector in time domain
J	=	coordinate transformation Jacobian
k	=	wave number, $2\pi/\lambda$
$\hat{\boldsymbol{n}}$	=	unit vector along normal direction
t	=	time
x, y, z	=	Cartesian coordinates
β	=	incident wave angle
ε	=	electric permittivity coefficient
ξ, η, ζ	=	generalized body-fitted coordinates
λ	=	wavelength
μ	=	magnetic permeability coefficient
σ	=	radar cross section

Subscripts

i, j, k	=	discrete spatial index
t	=	partial differentiation with respect to t
x, y, z	=	partial differentiation with respect to x, y, z
ξ, η, ζ	=	partial differentiation with respect to ξ, η, ζ
0	=	free-space value

Superscripts

i	=	incident-field value
n	=	discrete time index
s	=	scattered-field value
x, y, z	=	components in x, y, z directions

Presented as Paper 95-1950 at the AIAA 26th Plasmadynamics and Lasers Conference, San Diego, CA, June 19–22, 1995; received Sept. 5, 1995; revision received Sept. 23, 1996; accepted for publication Nov. 1, 1996.

*Research Scientist, 28 Research Drive. Member AIAA.
†Professor, Department of Mechanical and Aeronautical Engineering. Senior Member AIAA.

Introduction

UNTIL recently, aerodynamic efficiency has been the main objective in aircraft design. However, as evidenced by the introduction of the Lockheed F-117A and the Northrop B-2, it is clear that in addition to aerodynamic efficiency, today's aircraft designers are also concerned with radar cross section (RCS) reduction to enhance the survivability of military aircraft. The latter objective of this multidisciplinary design problem requires accurate and efficient modeling of electromagnetic scattering. This requirement, in turn, necessitates the use of computational electromagnetics (CEM) in aircraft design.

References 1 and 2 present an excellent overview of the electromagnetic scattering mechanisms typical for aircraft as well as the various mathematical models available for RCS prediction. The conventional approach to modeling electromagnetic scattering has been the use of frequency-domain techniques, namely, high-frequency asymptotic methods (geometrical optics, physical optics, geometrical theory of diffractions, physical theory of diffractions, etc.),[3] and the method of moments.[4] High-frequency methods are the traditional RCS prediction techniques used in aircraft design and have until recently provided the only practical means of analyzing electromagnetic scattering from electrically large objects (i.e., objects with characteristic dimensions much larger than the illuminating wavelength). However, these relatively simple methods rely on approximations that neglect small, but often important, physical features of the scattering object in addition to many detailed electromagnetic phenomena such as tip and edge diffractions, interference and polarization effects, creeping waves, etc. Consequently, high-frequency methods provide only a first-order approximation of the RCS. The method of moments is similar to the panel method used in aerodynamic analysis. It is more accurate than high-frequency techniques, but for problems involving electrically large scattering objects this method is computationally expensive because of the required inversion of very large matrices. This is because the surface patches must be relatively small (of the order of 0.1–0.2 wavelength) to maintain accuracy. Even with the current supercomputers, analysis of a complete aircraft using the method of moments is not feasible for radar frequencies much higher than 150 MHz. Considering that modern radars operate at frequencies as high as 20 GHz with corresponding wave-

lengths as small as 0.015 m, this method tends to be impractical for use in aircraft design.

As an alternative, researchers have begun to consider computational methods based on field approximation of the time-domain Maxwell's equations. This approach offers significant advantages over the conventional modeling techniques described earlier. First, field methods based on finite difference, finite element, and finite volume discretizations are highly accurate and require significantly less computational effort to simulate scattering from electrically large objects than the method of moments. Second, unlike the frequency-domain approach, the time-domain formulation of Maxwell's equations allows the computation of transient and particular responses to both single-frequency harmonic waves as well as a multifrequency single pulse. In addition to these advantages, a major attractive feature of the field approach is that a large number of discretization techniques that have been developed and used extensively in computational fluid dynamics (CFD) can be applied directly to CEM. This allows a synergistic approach to solve the multidisciplinary problem of shape design for aerodynamic efficiency and low observability.

At the present time, several researchers have developed time-domain Maxwell solvers based on various field discretization techniques: finite difference,[5–7] finite volume,[8–10] and finite element.[11,12] The finite difference scheme proposed by Yee[5] in 1966 was the first field method developed for modeling electromagnetic scattering in the time domain. It uses leapfrog time integration to integrate Maxwell's equations on staggered Cartesian grids. This scheme is often referred to as the FDTD (finite difference time domain) method and has been applied to analyze a wide range of scattering problems, mainly by the traditional electromagnetic research community. An excellent review of these studies is presented in Ref. 6. Because of the lack of established alternative algorithms, the Yee scheme[5] is currently the most widely used field method for solving the time-dependent Maxwell's equations. Despite its popularity, however, this scheme has several drawbacks. First, the stair-stepped approximation of curved boundaries resulting from the use of Cartesian grids often leads to poor modeling of complex body shapes unless very dense grids are used. This is because the nonconforming rectangular grid makes it difficult to accurately impose surface boundary conditions. In addition, the use of staggered grids requires complicated programming logic, especially for problems involving complex three-dimensional geometries. These difficulties can be avoided with the use of nonstaggered numerical schemes in conjunction with body-fitted curvilinear grids as is commonly done in CFD. This approach was first applied to CEM by Shankar et al.[8] and has been shown to be very effective in modeling complex scattering problems.

This paper presents an alternative finite difference Maxwell solver for the numerical simulation of electromagnetic scattering from three-dimensional arbitrarily shaped objects. The work described here is an extension of previous research performed by the authors.[13–15] It represents an effort aimed at developing an accurate and efficient method for RCS prediction. The current Maxwell solver uses an explicit, second-order accurate, central-difference scheme to solve the time-dependent Maxwell's equations on nonstaggered, body-fitted grids. This formulation offers the advantages of the time-domain field approach to modeling electromagnetic scattering while avoiding the drawbacks associated with the popular FDTD method. In the following sections, a description of the finite difference formulation and the postprocessing procedures for transforming field solutions of Maxwell's equations into RCS are described. Next, results of two test cases are presented to illustrate the accuracy of the present Maxwell solver. Finally, a parametric study showing the effects of shaping on the RCS of typical aircraft wing configurations is presented. This parametric study illustrates the effectiveness of the Maxwell solver as an analysis and design tool.

Maxwell's Equations

In an isotropic and source-free medium with linear properties, electromagnetic wave propagation is governed by Maxwell's equations:

Ampere's law:

$$(\varepsilon \boldsymbol{E})_t - \nabla \times \boldsymbol{H} = 0 \tag{1}$$

Faraday's law:

$$(\mu \boldsymbol{H})_t + \nabla \times \boldsymbol{E} = 0 \tag{2}$$

For scattering problems, $\boldsymbol{E}$ and $\boldsymbol{H}$ represent total fields that are composed of incident and scattered components. Because of the linearity of Maxwell's equations, the total fields can be written as $\boldsymbol{E} = \boldsymbol{E}^i + \boldsymbol{E}^s$ and $\boldsymbol{H} = \boldsymbol{H}^i + \boldsymbol{H}^s$. Noting that the incident wave always propagates in free space, Eqs. (1) and (2) can be rewritten in terms of scattered fields[16]:

Ampere's law:

$$(\varepsilon \boldsymbol{E}^s)_t - \nabla \times \boldsymbol{H}^s = [(\varepsilon_0 - \varepsilon)\boldsymbol{E}^i]_t$$

Faraday's law:

$$(\mu \boldsymbol{H}^s)_t + \nabla \times \boldsymbol{E}^s = [(\mu_0 - \mu)\boldsymbol{H}^i]_t$$

Note that in free space, the total- and scattered-field forms of Maxwell's equations are identical.

To facilitate the implementation of numerical schemes, Eqs. (1) and (2) are rewritten in vector form as follows:

$$\bar{\boldsymbol{Q}}_t + \bar{\boldsymbol{R}}_x + \bar{\boldsymbol{S}}_y + \bar{\boldsymbol{T}}_z = 0 \tag{3}$$

where

$$\bar{\boldsymbol{Q}} = [\varepsilon E^x, \varepsilon E^y, \varepsilon E^z, \mu H^x, \mu H^y, \mu H^z]^t$$

$$\bar{\boldsymbol{R}} = [0, H^z, -H^y, 0, -E^z, E^y]^T$$

$$\bar{\boldsymbol{S}} = [-H^z, 0, H^x, E^z, 0, -E^x]^T$$

$$\bar{\boldsymbol{T}} = [H^y, -H^x, 0, -E^y, E^x, 0]^T$$

In general, surfaces of complex-shaped objects cannot be modeled adequately in the Cartesian coordinate system. In regions of high curvature, the use of rectangular coordinates results in stair-stepped representations of smooth surfaces, thus making it difficult to accurately impose surface boundary conditions. For electromagnetic scattering applications, particularly RCS prediction, it is essential that all high-gradient regions along the surface of the scattering object are properly resolved to accurately model the scattering physics. This can be achieved only with the body-fitted curvilinear coordinate system. As a result of the transformation to a body-fitted curvilinear coordinate system (see Ref. 16 for details), Eq. (3) becomes

$$\boldsymbol{Q}_t + \boldsymbol{R}_\xi + \boldsymbol{S}_\eta + \boldsymbol{T}_\zeta = 0 \tag{4}$$

where

$$\boldsymbol{Q} = \frac{1}{J}\begin{bmatrix} \varepsilon E^x \\ \varepsilon E^y \\ \varepsilon E^z \\ \mu H^x \\ \mu H^y \\ \mu H^z \end{bmatrix} \qquad \boldsymbol{R} = \frac{1}{J}\begin{bmatrix} \xi_z H^y - \xi_y H^z \\ \xi_x H^z - \xi_z H^x \\ \xi_y H^x - \xi_x H^y \\ \xi_y E^z - \xi_z E^y \\ \xi_z E^x - \xi_x E^z \\ \xi_x E^y - \xi_y E^x \end{bmatrix}$$

$$\boldsymbol{S} = \frac{1}{J}\begin{matrix}\eta_z H^y - \eta_y H^z \\ \eta_x H^z - \eta_z H^x \\ \eta_y H^x - \eta_x H^y \\ \eta_y E^z - \eta_z E^y \\ \eta_z E^x - \eta_x E^z \\ \eta_x E^y - \eta_y E^x\end{matrix} \qquad \boldsymbol{T} = \frac{1}{J}\begin{matrix}\zeta_z H^y - \zeta_y H^z \\ \zeta_x H^z - \zeta_z H^x \\ \zeta_y H^x - \zeta_x H^y \\ \zeta_y E^z - \zeta_z E^y \\ \zeta_z E^x - \zeta_x E^z \\ \zeta_x E^y - \zeta_y E^x\end{matrix}$$

Here, $\xi = \xi(x, y, z)$ and $\eta = \eta(x, y, z)$ denote the circumferential coordinates tangent to the body, and $\zeta = \zeta(x, y, z)$ denotes the radial coordinate. The transformation metrics and Jacobian are defined as

$$\xi_x = J[y_\eta z_\zeta - y_\zeta z_\eta] \quad \eta_x = J[y_\zeta z_\xi - y_\xi z_\zeta] \quad \zeta_x = J[y_\xi z_\eta - y_\eta z_\xi]$$

$$\xi_y = J[x_\zeta z_\eta - x_\eta z_\zeta] \quad \eta_y = J[x_\xi z_\zeta - x_\zeta z_\xi] \quad \zeta_y = J[x_\eta z_\xi - x_\xi z_\eta]$$

$$\xi_z = J[x_\eta y_\zeta - x_\zeta y_\eta] \quad \eta_z = J[x_\zeta y_\xi - x_\xi y_\zeta] \quad \zeta_z = J[x_\xi y_\eta - x_\eta y_\xi]$$

$$J = 1/(x_\xi y_\eta z_\zeta + x_\eta y_\zeta z_\xi + x_\zeta y_\xi z_\eta - x_\xi y_\zeta z_\eta - x_\eta y_\xi z_\zeta - x_\zeta y_\eta z_\xi)$$

The vectors $\boldsymbol{R}$, $\boldsymbol{S}$, and $\boldsymbol{T}$ can be written as functions of vector $\boldsymbol{Q}$ as follows:

$$\boldsymbol{R} = A\boldsymbol{Q} \qquad \boldsymbol{S} = B\boldsymbol{Q} \qquad \boldsymbol{T} = C\boldsymbol{Q} \tag{5}$$

where

$$A = \begin{matrix} 0 & 0 & 0 & 0 & \frac{\xi_z}{\mu} & \frac{\xi_y}{\mu} \\ 0 & 0 & 0 & -\frac{\xi_z}{\mu} & 0 & \frac{\xi_x}{\mu} \\ 0 & 0 & 0 & \frac{\xi_y}{\mu} & \frac{\xi_x}{\mu} & 0 \\ 0 & -\frac{\xi_z}{\varepsilon} & \frac{\xi_y}{\varepsilon} & 0 & 0 & 0 \\ \frac{\xi_z}{\varepsilon} & 0 & -\frac{\xi_x}{\varepsilon} & 0 & 0 & 0 \\ -\frac{\xi_y}{\varepsilon} & \frac{\xi_x}{\varepsilon} & 0 & 0 & 0 & 0 \end{matrix}$$

$$B = \begin{matrix} 0 & 0 & 0 & 0 & \frac{\eta_z}{\mu} & \frac{\eta_y}{\mu} \\ 0 & 0 & 0 & -\frac{\eta_z}{\mu} & 0 & \frac{\eta_x}{\mu} \\ 0 & 0 & 0 & \frac{\eta_y}{\mu} & \frac{\eta_x}{\mu} & 0 \\ 0 & -\frac{\eta_z}{\varepsilon} & \frac{\eta_y}{\varepsilon} & 0 & 0 & 0 \\ \frac{\eta_z}{\varepsilon} & 0 & -\frac{\eta_x}{\varepsilon} & 0 & 0 & 0 \\ -\frac{\eta_y}{\varepsilon} & \frac{\eta_x}{\varepsilon} & 0 & 0 & 0 & 0 \end{matrix}$$

$$C = \begin{matrix} 0 & 0 & 0 & 0 & \frac{\zeta_z}{\mu} & \frac{\zeta_y}{\mu} \\ 0 & 0 & 0 & -\frac{\zeta_z}{\mu} & 0 & \frac{\zeta_x}{\mu} \\ 0 & 0 & 0 & \frac{\zeta_y}{\mu} & \frac{\zeta_x}{\mu} & 0 \\ 0 & -\frac{\zeta_z}{\varepsilon} & \frac{\zeta_y}{\varepsilon} & 0 & 0 & 0 \\ \frac{\zeta_z}{\varepsilon} & 0 & -\frac{\zeta_x}{\varepsilon} & 0 & 0 & 0 \\ -\frac{\zeta_y}{\varepsilon} & \frac{\zeta_x}{\varepsilon} & 0 & 0 & 0 & 0 \end{matrix}$$

Equation (4) represents a system of hyperbolic equations that can be solved numerically using any one of the numerous CFD-based finite difference schemes. The present Maxwell solver uses the classical Lax–Wendroff scheme. This explicit scheme is second-order accurate in both time and space, and it does not require the computational grid to be staggered. Although implicit schemes would allow the use of larger time steps, they also produce more dispersion or phase error than explicit schemes.[13] For problems involving electromagnetic-wave propagation, it is critical that the phase error is kept to a minimum to maintain accuracy.

Lax–Wendroff Scheme

The Lax–Wendroff algorithm for Eq. (4) is derived starting from the Taylor-series expansion of vector $\boldsymbol{Q}$ about discrete point i, j, k and time level n:

$$\boldsymbol{Q}^{n+1}_{i,j,k} = \boldsymbol{Q}^{n}_{i,j,k} + \Delta t \boldsymbol{Q}_t + (\Delta t^2/2)\boldsymbol{Q}_{tt} + \mathcal{O}(\Delta t^3) \tag{6}$$

The second-order time derivative is retained to achieve second-order accuracy and to provide coupling between adjacent grid points. Using Eq. (4), the time derivatives on the right-hand side (RHS) of Eq. (6) are replaced with spatial derivatives. For the first-order time derivative, this is trivial:

$$\boldsymbol{Q}_t = -(\boldsymbol{R}_\xi + \boldsymbol{S}_\eta + \boldsymbol{T}_\zeta) \tag{7}$$

For the second-order time derivative, this can be done by first taking the derivative of Eq. (7) with respect to time and then replacing $\boldsymbol{R}$, $\boldsymbol{S}$, and $\boldsymbol{T}$ with Eq. (5). The result is

$$\boldsymbol{Q}_{tt} = -[(A\boldsymbol{Q}_t)_\xi + (B\boldsymbol{Q}_t)_\eta + (C\boldsymbol{Q}_t)_\zeta] \tag{8}$$

Note that the Jacobian matrices A, B, and C are independent of time, but are functions of ξ, η, and ζ. The next step is to replace the time derivatives on the RHS of Eq. (8) with Eq. (7):

$$\boldsymbol{Q}_{tt} = (AF)_\xi + (BF)_\eta + (CF)_\zeta \tag{9}$$

where

$$F = \boldsymbol{R}_\xi + \boldsymbol{S}_\eta + \boldsymbol{T}_\zeta$$

The time derivatives in Eq. (6) can now be eliminated using Eqs. (7) and (9):

$$\boldsymbol{Q}^{n+1}_{i,j,k} = \boldsymbol{Q}^{n}_{i,j,k} - \Delta t F + (\Delta t^2/2)[(AF)_\xi + (BF)_\eta + (CF)_\zeta] \tag{10}$$

The final form of the Lax–Wendroff scheme for Maxwell's equations is obtained by replacing all spatial derivatives in Eq. (10) with central differences.

Boundary Conditions

Numerical simulation of electromagnetic scattering entails solving the discrete Maxwell's equations on a computational grid that covers the surface of the scattering object and extends to some finite distance away from the scattering object where it is terminated. The truncated computational domain is necessary because of the limited memory available on computers used to perform the simulation. At the inner boundary that conforms to the scattering surface, reflecting boundary conditions are imposed to numerically simulate the reflection and transmission of impinging electromagnetic waves. At the outer boundary, an absorbing boundary condition is specified to allow scattered waves to propagate out of the computational domain.

Absorbing Boundary Condition

A one-dimensional characteristic boundary condition[17] is imposed at the outer boundary:

$$W_t + c(W_\zeta/R_\zeta) = 0 \tag{11}$$

where $W = [E^x, E^y, E^z, H^x, H^y, H^z]^T$, $c = 1/\sqrt{\varepsilon\mu}$ is the wave speed, ζ is the coordinate normal to the outer boundary, and R is the radial distance along the ζ direction. This absorbing boundary condition assumes that scattered waves propagate in the direction normal to the outer boundary as they leave the computational domain. In reality, scattered waves can propagate in any arbitrary direction as they approach the outer boundary and, consequently, Eq. (11) allows scattered waves to reflect from the outer boundary back into the computational domain. However, since scattered waves decay by a factor of $1/\sqrt{R}$ and $1/R$ in two and three dimensions, respectively, as they propagate away from the scattering object,[18] the amount of reflection can be minimized by placing the outer boundary sufficiently far away from the scattering object.

Reflecting Boundary Conditions

The present study considers only scattering from perfect electric conductors that reflect, but do not transmit, impinging electromagnetic waves. The surface boundary conditions for this case are[19]

$$\hat{\boldsymbol{n}} \times \boldsymbol{E} = 0 \tag{12}$$

$$\hat{\boldsymbol{n}} \cdot \boldsymbol{H} = 0 \tag{13}$$

Equations (12) and (13) imply that the tangential components of the total electric field intensity and the normal component of the total magnetic field intensity vanish at the body.

In general, it is more advantageous to solve Maxwell's equations in terms of the scattered-field formulation. In the total-field formulation, the incident wave must be propagated numerically through the computational domain. Because of the dispersive nature of most numerical schemes, waves become distorted as they are numerically propagated through a non-uniform, curvilinear grid. To minimize dispersion error, the present Maxwell solver was developed using the scattered-field formulation in which the incident electric and magnetic fields are propagated analytically and only the scattered fields are computed. This approach has the additional advantage in that the scattered field, which has a lower amplitude than the total field, can be more easily absorbed by the absorbing boundary condition, thus resulting in less reflection at the outer boundary. To enforce the total-field reflecting boundary conditions (12) and (13), total fields are computed at the body and the incident fields, which are known analytically, and are then subtracted out to obtain the scattered fields before the solution is advanced to the next time level. Therefore, in the scattered-field formulation, the effects of the incident wave are introduced through the reflecting boundary conditions. The scattering object in this case acts as a radiating body.

RCS

RCS is a measure of the intensity of the scattered electromagnetic waves with respect to the impinging signal. When the radar transmitter and receiver are located at the same location, the observed RCS is known as backscatter or monostatic RCS. When the directions of illumination and observation are not collocated, the resulting RCS is called bistatic RCS. The bistatic RCS is defined as

$$\sigma = \lim_{\boldsymbol{R}\to\infty} 4\pi|\boldsymbol{R}|^2 \frac{|\tilde{\boldsymbol{E}}^s(\boldsymbol{R})|^2}{|\tilde{\boldsymbol{E}}^i|^2}$$

where the vector quantities $\tilde{\boldsymbol{E}}^s$ and $\tilde{\boldsymbol{E}}^i$ represent the complex Fourier components of the scattered and incident electric field intensities, respectively, and $\boldsymbol{R}$ denotes the vector from the scattering object to the observation point located in free space. Note that RCS is defined in the frequency domain. Therefore, the computed solution of the time-domain Maxwell's equations must be transformed into frequency domain to calculate RCS. In the present study, time-dependent solutions are saved over one complete wave cycle after time-harmonic steady state has been reached. The time-domain solutions are then transformed into frequency domain using fast Fourier transform. In addition, note that the scattered electric field intensity is a function of $\boldsymbol{R}$ and RCS is defined for $\boldsymbol{R}$ approaching infinity. Since the computational domain is finite, only scattered fields near the scattering object are computed. This so-called near-field solution must be transformed to the far-field solution before RCS can be computed. Using Green's function transform, the bistatic RCS becomes[20]

$$\sigma = (1/4\pi)|S|^2$$

where

$$S = \frac{1}{|\tilde{E}^i|}\int_C [(\hat{\boldsymbol{n}}\cdot\tilde{\boldsymbol{E}})\hat{\boldsymbol{k}} + (\hat{\boldsymbol{n}}\times\tilde{\boldsymbol{E}})\times\hat{\boldsymbol{k}} + j\hat{\boldsymbol{n}}\times(\nabla\times\tilde{\boldsymbol{E}})]e^{-j\hat{\boldsymbol{k}}\cdot\boldsymbol{r}'}\,dC$$

Here, C represents the integration path around the scattering object, $\hat{\boldsymbol{k}} = k\boldsymbol{R}/|\boldsymbol{R}|$, $j = \sqrt{-1}$ is the complex number, and $\boldsymbol{r}'$ represents the vector from the origin of the coordinate system to a point on C.

CEM Simulation

In the present study, only scatterings from perfect electric conductors in free space are simulated. The scattered-field formulation is used with ε_0 and μ_0 normalized to unity. Each simulation starts from zero scattered fields everywhere and is run until the scattered fields reach time-harmonic steady state. To minimize dissipation and dispersion errors, a time step corresponding to Courant–Friedrich–Lewy (CFL) = 1 (based on the smallest grid spacing) is used in all simulations. Incident electromagnetic waves are modeled as sinusoidal plane waves defined as

$$E^{z,i} = E_0 \sin[k(x\cos\beta + y\sin\beta - c_0 t)]$$

$$H^{x,i} = \frac{E^{z,i}\sin\beta}{\mu_0 c_0} \qquad H^{y,i} = -\frac{E^{z,i}\cos\beta}{\mu_0 c_0}$$

One of the most important issues in numerical simulation is grid resolution. In CEM, proper grid resolution depends not only on the body dimensions, but also on the wavelength, since electromagnetic waves must be properly resolved. Otherwise

numerical errors will cause propagating waves to become severely distorted. In the course of validating the present Maxwell solver, it was found that a grid resolution of at least 10 grid points per wavelength is required to accurately resolve a wave. For problems involving wave scattering from a single object, this grid resolution is necessary only on and near the body, where the scattering occurs, provided the scattered-field formulation is used. If the total-field formulation is used, proper grid resolution must be maintained over the entire region required to propagate the incident wave to the scattering object. Similarly, when multiple scattering between several objects are involved, the computational grid must be properly resolved in regions between the scattering objects to accurately propagate scattered waves from one object to another, regardless of which field formulation is used.

Code Validation

The present Maxwell solver has been validated for two test cases: 1) the standard sphere and 2) the more realistic aircraft wing. The results are presented to illustrate the accuracy of the solver.

Sphere

The first test case is a sphere with an electrical size of $ka = 3.5$ where a is the sphere radius. The circumference of the sphere is 3.5λ, where $\lambda = \pi/3.5$. The sphere is illuminated by a horizontally polarized plane wave propagating along the positive x direction as follows:

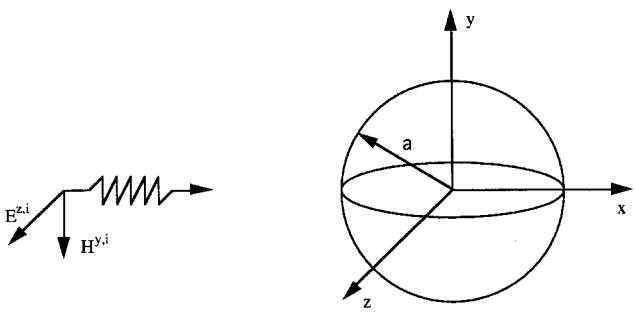

The computational grid for this case contains 61 and 31 points in the two circumferential directions ξ and η, respectively, and 40 points in the radial or ζ direction for a total of $61 \times 31 \times 40$ points. The outer grid boundary is located approximately 3λ from the sphere surface. The minimum grid resolution on the surface is roughly 17 points per wavelength. In the radial direction, the grid is stretched with a resolution of approximately 22 points per wavelength next to the surface and roughly 9 points per wavelength at the outer boundary. A close-up view of the surface and volume grids is shown in Fig.

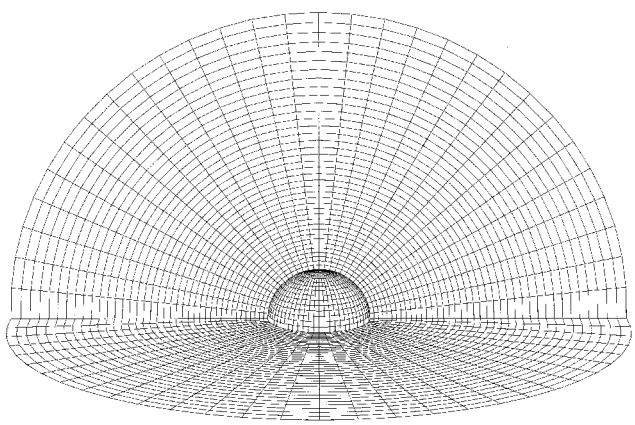

Fig. 1 Close-up view of computational grid for the sphere.

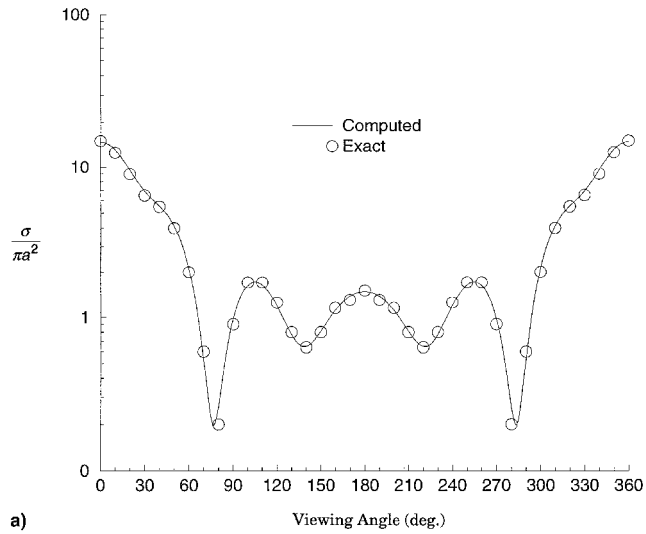

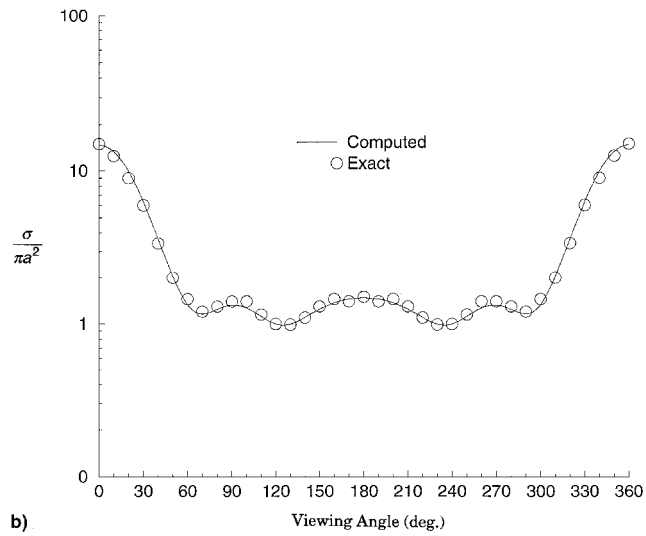

Fig. 2 Bistatic RCS of the sphere in the a) *xz* and b) *xy* planes ($ka = 3.5$).

1. The scattering is simulated for five wave cycles with field variables collected in the fifth cycle for RCS calculation.

Before results are presented for this test case, it is necessary to discuss the treatment of the pole singularity. The pole singularity arises from the fact that grid points at the pole of the sphere collapse onto a single point (see Fig. 1), resulting in zero volume. As a result, the transformation Jacobian, which represents the inverse of the volume, becomes infinite at the pole. The infinite Jacobian presents a problem in that it causes variables in the transformed Maxwell's equations [see Eq. (4)] to be undefined at the pole. This singularity occurs all along the pole axis that extends from the surface of the sphere to the outer grid boundary. The current Maxwell solver treats this problem by not solving the governing equations along the pole axis. Field variables along the pole axis are obtained by averaging values from surrounding grid points on the ζ = const surface.

The computed bistatic RCS of the sphere in the xz and xy planes are compared against the exact solutions[21] in Fig. 2. Here, viewing angles are measured counterclockwise from the positive x axis. Thus, the 0-/360-deg viewing angle corresponds to forward scattering, whereas the 180-deg viewing angle indicates backscattering. Overall, the computed RCS in the two viewing planes are in excellent agreement with the exact solutions.

Aircraft Wing

The second test case is a unswept rectangular wing with a uniform spanwise thickness distribution (except near the collapsed tip). The wing is composed of the NACA 0012 airfoil sections. It has a chord length of $c = 1.0$ and a wing span of $b = 2.0$. The wing is illuminated head-on (0-deg incidence) by a horizontally polarized plane wave with a wavelength of $\lambda = 0.5c$ as follows:

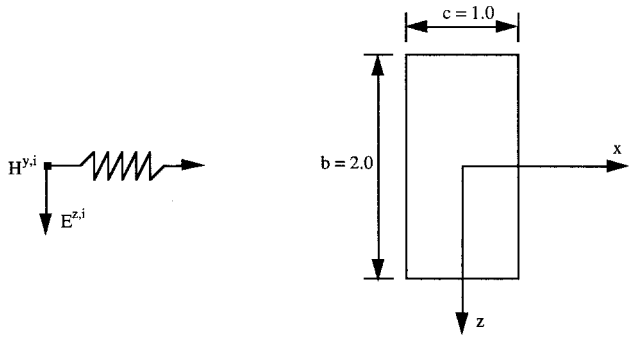

An O–H topology grid is used to discretize the computational domain. The surface grid consists of 59 airfoil sections in the spanwise direction (49 on the wing) with 101 points around each airfoil section. The volume grid is created by generating an O grid around each airfoil section and connecting it to its spanwise neighbor to form the O–H grid. The resulting grid contains 41 points in the radial direction for a total of 101 × 59 × 41 points with the outer boundary located approximately 2λ from the wing. The grid has a resolution of at least 10 points per wavelength on and near the wing. A close-up view of the surface and volume grids is shown in Fig. 3. Note that the airfoil section at the wingtip is collapsed to zero thickness. This collapsed profile is maintained outboard of the wingtip along the spanwise direction with geometric stretching to the outer boundary. In the current simulation, the governing equations are not solved on the collapsed plane between the wingtip and outer boundary. Instead, the solution on this plane is obtained by averaging values from grid points located directly above and below the collapsed plane. Note that the entire wing has to be simulated since some field components are 180 deg out of phase about the spanwise symmetry plane.

The scattering is simulated for five wave cycles with field variables collected in the fifth cycle for RCS analysis. The computed bistatic RCS in the *xy* plane is shown in Fig. 4a along with the scaled method of moments solution for the NACA 0012 airfoil. In general, the RCS of an infinitely long cylinder can be scaled to approximate the RCS of a cylinder of length L with the same cross-sectional shape using the following scaling factor[22]:

$$\sigma_{3D} = [2L^2/\lambda]\sigma_{2D}$$

In the case of aircraft wings, this equation gives a fairly accurate approximation of the RCS for unswept rectangular wings based on the RCS of an infinite wing having the same airfoil section (i.e., the RCS of the airfoil itself). Note that this scaling relation is invalid if the wing is swept or if the airfoil shape/dimension changes along the spanwise direction. As shown in Fig. 3a, the computed bistatic RCS of the three-dimensional wing is in good agreement with the scaled method-of-moments solution for the two-dimensional airfoil. The computed bistatic RCS in the *xz* plane is shown in Fig. 4b. Again, viewing angles are measured counterclockwise from the positive *x* axis. Note that for military aircraft, the bistatic RCS in the *xy* plane is the most informative since it contains simultaneously the RCS in the four most threatening directions: rear, front, above, and below, which correspond to viewing angles of 0/360, 180, 90, and 270 deg, respectively.

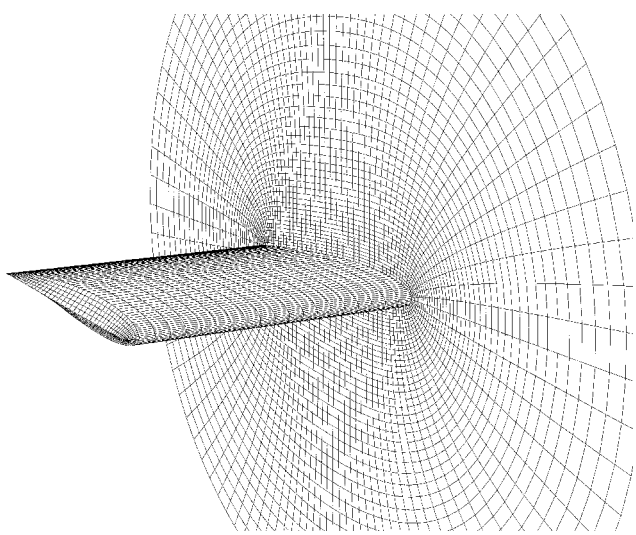

Fig. 3 Close-up view of computational grid for the rectangular wing.

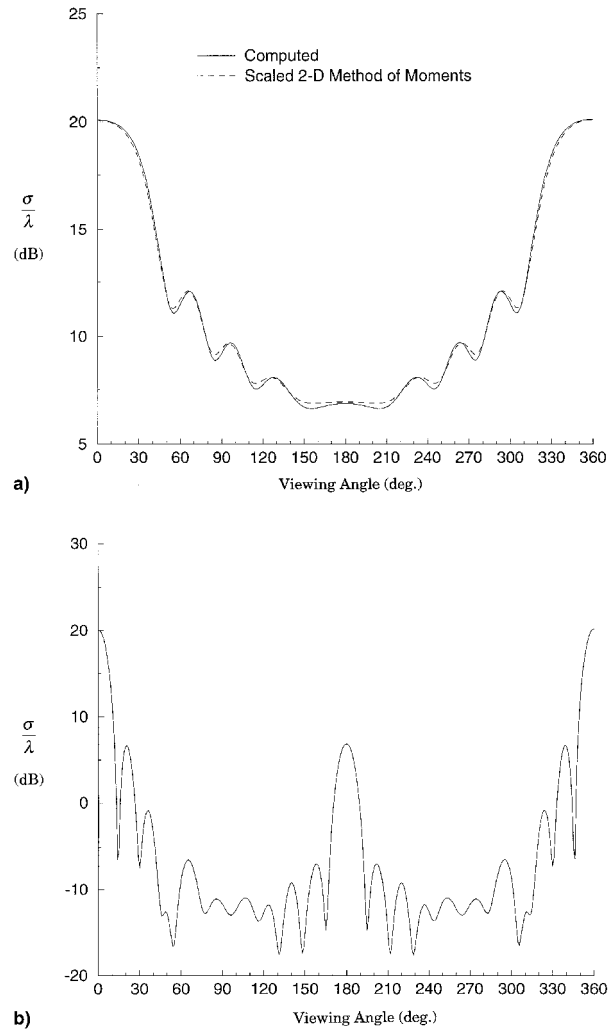

Fig. 4 Bistatic RCS of the rectangular wing in the a) *xy* and b) *xz* planes.

Parametric Study

In the previous section, the accuracy of the Maxwell solver was demonstrated for two arbitrarily shaped objects. In this

section, the capability of the Maxwell solver as a design and analysis tool is demonstrated by applying the solver to analyze the observability of various aircraft wing configurations. Specifically, the effects of systematic changes in the shape of aircraft wings on the RCS based on head-on radar illumination are examined. As noted earlier, knowledge of the bistatic RCS in the *xy* plane is more critical than in the other two viewing planes and, consequently, only the effects of shape changes on the RCS in the *xy* plane are considered. All simulations are performed using the same grid parameters and incident-wave conditions as those described in the previous section.

Effect of Spanwise Thickness Distribution

In this study, the effect of spanwise thickness distribution on the RCS of aircraft wings is examined. The study compares the RCS of two wings: one with a uniform thickness distribution along the spanwise direction (except near the collapsed tip) and one with a variable spanwise thickness distribution. The unswept rectangular wing described in the previous section is used as the baseline wing. This baseline wing is modified by linearly decreasing its spanwise thickness between the root and tip such that the maximum thickness near the collapsed tip is half the maximum thickness at the root (i.e., a 2:1 root-to-tip thickness ratio).

The computed bistatic RCS of the baseline and modified wings are compared in Fig. 5. Note that only a slight reduction in the RCS has been achieved in and around the backscattering direction (180-deg viewing angle) by varying the spanwise thickness. Of course, more reduction in the RCS can be attained by further decreasing the wing thickness between the root and tip or by simply using a thinner airfoil section for the entire wing as suggested by the result of a previous parametric study of airfoils.[23] However, because of possible design constraints on the aerodynamic performance, structural integrity, and fuel-carrying capacity of the wing, these options may not be viable.

Effect of Wing Sweep

This study examines the effect of sweeping on the observability of aircraft wings by comparing the RCS of a rectangular wing with and without sweep. To maintain the same wing span between the unswept and swept configurations, the wing is actually not swept, but is sheared by an angle θ as illustrated as follows:

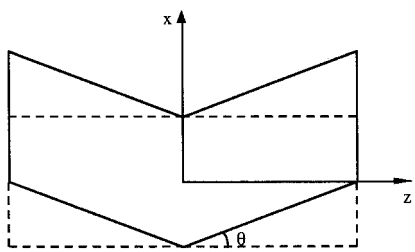

Here the term swept is used loosely to describe the sheared configuration. Again, the unswept, rectangular wing described in the code validation section is used as the baseline configuration. The computed bistatic RCS of the wing with 0-, 5-, and 10-deg sweeps are compared in Fig. 6. These results show that a significant reduction of the RCS in and around the backscattering direction can be achieved with only a small amount of sweep. Thus, compared to varying the spanwise thickness, sweeping the wing is a better method for reducing the radar signature, since a large reduction in the RCS can be attained without requiring any changes to the wing basic dimensions. By maintaining the basic dimensions of the unswept wing, the original requirements on the aerodynamic performance, structural integrity, and fuel-carrying capacity of the wing can still be satisfied. Note that further reduction in the RCS can be achieved as shown in Fig. 6 by also varying the spanwise thickness of the wing in addition to the use of wing sweep.

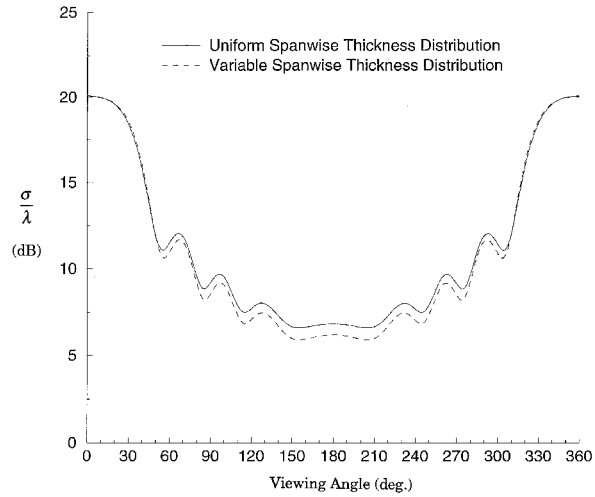

Fig. 5 Effect of spanwise thickness on the bistatic RCS.

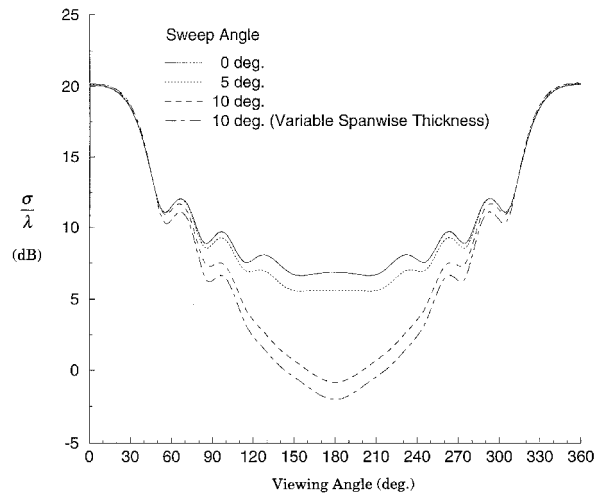

Fig. 6 Effect of wing sweep on the bistatic RCS.

Finally, it should be noted that sweeping a wing will increase its bistatic RCS in the spanwise direction since the incident wave will be deflected more toward the side. However, the RCS of a wing or any other aircraft configurations cannot be reduced for all possible threat directions except through the use of radar-absorbing materials or coatings. Thus, a tradeoff decision has to be made and a typical low-observable configuration can be designed to minimize only the threat in a preselected direction. For head-on radar illumination, the use of wing sweep will only reduce the return signal toward the front of the wing.

Conclusions

The development and application of a finite difference algorithm for the numerical simulation of electromagnetic scattering have been presented. The current algorithm solves the time-dependent Maxwell's equations on nonstaggered, body-fitted grids using the explicit, second-order-accurate Lax–Wendroff scheme that has been developed and used extensively in CFD. The time-domain formulation of Maxwell's equations allows the computation of transient and particular responses to both single-frequency harmonic waves as well as a multifrequency single pulse. The use of body-fitted grids in combination with the Lax–Wendroff scheme results in an accurate and efficient numerical algorithm capable of simulating electromagnetic scattering from electrically large objects while

avoiding the drawbacks associated with the use of staggered Cartesian grids employed by the traditional FDTD method. It also allows a synergistic approach to solve the multidisciplinary problem of shape design for aerodynamic efficiency and low observability.

Results of the validation study show that the current Maxwell solver is very accurate in predicting the bistatic RCS of arbitrarily shaped objects. The capability of the Maxwell solver as a design and analysis tool has also been demonstrated through a simple parametric study that examined the effects of systematic changes in the shapes of aircraft wings on their RCS. The results indicate that for head-on radar illumination, a significant reduction in the RCS of a wing can be achieved by sweeping its leading edge and varying its spanwise thickness. Although designers could deduce these results intuitively, the current Maxwell solver allows them to quantify the effects of shaping on the RCS of an aircraft configuration and to balance aircraft observability against other design criteria such as aerodynamic performance, structural integrity, and fuel-carrying capacity.

Acknowledgment

This research was partially funded by the NASA Ames Research Center through Joint Research Interchange Agreement NCA2-568 and NCA2-581.

References

[1]Stadmore, H. A., "Radar Cross Section Fundamentals for the Aircraft Designer," AIAA Paper 79-1818, Aug. 1979.

[2]Hitzel, S. M., "Aerodynamics and Radar Signature: A Combination of Theoretical Methods," *Journal of Aircraft*, Vol. 25, No. 5, 1988, pp. 399–404.

[3]Knott, E. F., "Radar Cross Section," *Aspects of Modern Radar*, edited by E. Brookner, Artech House, Boston, MA, 1988, pp. 413–485.

[4]Umashankar, K. R., "Numerical Analysis of Electromagnetic Wave Scattering and Interaction Based on Frequency-Domain Integral Equation and Method of Moments Techniques," *Wave Motion*, Vol. 10, No. 6, 1988, pp. 493–525.

[5]Yee, K. S., "Numerical Solution of Initial Boundary Value Problems Involving Maxwell's Equations in Isotropic Media," *IEEE Transactions on Antennas and Propagation*, Vol. AP-14, No. 3, 1966, pp. 302–307.

[6]Taflove, A., "Review of the Formulation and Applications of the Finite-Difference Time Domain Method for Numerical Modeling of Electromagnetic Wave Interactions with Arbitrary Structures," *Wave Motion*, Vol. 10, No. 6, 1988, pp. 547–582.

[7]Goorjian, P. M., "Algorithm Development for Maxwell's Equations for Computational Electromagnetism," AIAA Paper 90-0251, Jan. 1990.

[8]Shankar, V., Hall, W. F., and Mohammadian, A. H., "A Time-Domain Differential Solver for Electromagnetic Scattering Problems," *Radar Cross Sections of Complex Objects*, edited by W. R. Stone, Inst. of Electrical and Electronic Engineers, New York, 1990, pp. 127–139.

[9]Shang, J. S., "A Characteristic-Based Algorithm for Solving 3-D, Time-Domain Maxwell Equations," AIAA Paper 92-0452, Jan. 1992.

[10]Huh, K. S., Shu, M., and Agarwal, R. K., "A Compact High-Order Finite-Volume Time Domain/Frequency-Domain Method for Electromagnetic Scattering," AIAA Paper 92-0453, Jan. 1992.

[11]Petitjean, B., and Lohner, R., "Finite Element Solvers for Radar Cross Section (RCS) Calculations," AIAA Paper 92-0455, Jan. 1992.

[12]Hafez, M., and English, P., "Application of Explicit Finite Element to Maxwell's Equations," *Proceedings of the 9th Annual Review of Progress in Applied Computational Electromagnetics*, Naval Postgraduate School, Monterey, CA, March 1993, pp. 838–845.

[13]Vinh, H., "An Investigation of the Numerical Characteristics of Finite-Difference Methods as Applied to the Time-Domain Maxwell's Equations," M.S. Thesis, Univ. of California, Davis, CA, Dec. 1991.

[14]Vinh, H., Dwyer, H. A., and Van Dam, C. P., "Finite-Difference Algorithms for the Time-Domain Maxwell's Equations — A Numerical Approach to RCS Analysis," AIAA Paper 92-2989, July 1992.

[15]Vinh, H., Dwyer, H. A., and Van Dam, C. P., "Finite-Difference Methods for Computational Electromagnetics (CEM)," *IEEE Antennas and Propagation Society International Symposium*, 1992 Digest, Vol. III, Chicago, IL, July 1992, pp. 1682–1695.

[16]Vinh, H., "Development of a Finite-Difference Time-Domain Solver for Maxwell's Equations with Application to Radar Signature Prediction," Ph.D. Dissertation, Univ. of California, Davis, CA, Dec. 1994.

[17]Mur, G., "Absorbing Boundary Conditions for the Finite-Difference Approximation of the Time-Domain Electromagnetic-Field Equations," *IEEE Transactions on Electromagnetic Compatibility*, Vol. EMC-23, No. 4, 1981, pp. 377–382.

[18]Knott, E. F., Shaeffer, J. F., and Tuley, M. T., *Radar Cross Section*, 2nd ed., Artech House, Boston, MA, 1993, p. 100.

[19]Crispin, J. W., and Siegel, K. M. (eds.), *Methods of Radar Cross Section Analysis*, Academic, New York, 1968, p. 4.

[20]Shankar, V., Hall, W. F., and Mohammadian, A. H., "A CFD-Based Finite-Volume Procedure for Computational Electromagnetics — Interdisciplinary Applications of CFD Methods," AIAA Paper 89-1987, June 1989.

[21]King, R., and Wu, T. T., *The Scattering and Diffraction of Waves*, Harvard Univ. Press, Cambridge, MA, 1959, p. 209.

[22]Shankar, V., Hall, W. F., Mohammadian, A. H., and Rowell, C., "Computational Electromagnetics (CEM): Development of a Finite-Volume, Time-Domain Solver for Maxwell's Equations," NASA Ames Research Center/Naval Air Development Center, Final Rept., Contract N62269-90-C-0257, 1993.

[23]Vinh, H., Van Dam, C. P., and Dwyer, H. A., "Airfoil Shaping for Reduced Radar Cross Section," *Journal of Aircraft*, Vol. 31, No. 4, 1994, pp. 787–793.